Available online at www.sciencedirect.com
ScienceDirect
Comput. Methods Appl. Mech. Engrg. 285 (2015) 714–729
Computer methods in applied mechanics and engineering
www.elsevier.com/locate/cma

Aeroelastic characteristics of functionally graded carbon nanotube-reinforced composite plates under a supersonic flow

S.A. Fazelzadeh*, S. Pouresmaeeli, E. Ghavanloo

School of Mechanical Engineering, Shiraz University, Shiraz 71963-16548, Iran

Received 11 May 2014; received in revised form 22 October 2014; accepted 28 November 2014
Available online 5 December 2014

Abstract

Aeroelastic characteristics of nanocomposite plates reinforced by carbon nanotubes and subjected to supersonic flow are investigated. Here, carbon nanotube-reinforced composite plates with five different distributions of carbon nanotube are considered. The material properties are supposed to vary gradually through the thickness of the plate and the rule of mixture is applied to estimate the effective material properties of nanocomposite plate. The governing equations of nanocomposite plate are derived based on Kirchhoff's plate theory and supersonic aerodynamic pressure is approximated by the first-order piston theory. Galerkin's method is utilized to obtain the solutions of the coupled governing equations, simultaneously. The suggested model is justified by a good agreement between the results given by present model and available data in the literature. To illustrate the effects of volume fraction, aspect ratio and non-dimensional in-plane forces on the aeroelastic stability of nanocomposite plates, parametric studies have been carried out.

Keywords: Aeroelastic characteristic; Nanocomposite; Functionally graded carbon nanotube-reinforced composite; Supersonic flow

1. Introduction

Aeroelastic phenomena are key factors in the design of modern structures such as space vehicles, high-speed aircrafts, skin sub-structures and gas turbine blades. These phenomena may strongly affect the performance of the structures. Therefore, many researchers have shown a great interest in both the static aeroelastic instability, known as divergence, and the dynamic aeroelastic instability, known as flutter.

In the past decades, new materials have been utilized to enhance the aeroelastic static and dynamic stabilities of the structures. Especially, the applications of functionally graded materials (FGMs) to the aeroelastic characteristics of the skin panels are found in several studies. Prakash and Ganapathi [1] studied the supersonic flutter of FGM rectangular flat plates subjected to two-dimensional static approximation of aerodynamic pressure in thermal environment. The nonlinear flutter and thermal buckling of FGM panels have been studied using nonlinear finite element method and first order shear deformation theory by Ibrahim et al. [2]. Aeroelastic stabilities of functionally graded panels

* Corresponding author. Tel.: +98 7116133238; fax: +98 7116473511.
E-mail address: Fazelzad@shirazu.ac.ir (S.A. Fazelzadeh).

http://dx.doi.org/10.1016/j.cma.2014.11.042
0045-7825/

subjected to aero-thermal loads have been studied [3] based on the first-order shear deformation theory and von Karman strain–displacement relation. Hosseini and Fazelzadeh [4] researched on aero-thermo-elastic post-critical and vibration characteristics of temperature-dependent FGM panels in a supersonic airflow. A review on the aero-thermo-elasticity of functionally graded panels can be found in [5].

In recent years, carbon nanotubes (CNTs) have attracted a great amount of attention due to their extraordinary mechanical properties. These exceptional properties such as, high elastic modulus, high tensile strength and stiffness, naturally make the CNTs to become a kind of most attractive reinforcement for nanocomposites [6–8]. Nanocomposites are a mixture of polymer matrix and CNTs as reinforcement of polymer composites. Extensive researches on the properties of carbon nanotube reinforced composites (CNTRCs) reveal that adding the CNTs even at very low volume fractions, improve mechanical properties of polymer matrices [9,10]. Distributions of the CNTs in the CNTRCs can be either uniform or functionally graded. The latter is well-known as functionally graded carbon nanotube-reinforced composite (FG-CNTRC). Similar to the FGMs, material properties of FG-CNTRC vary smoothly from one surface to the other. Due to significant properties of FG-CNTRC, mechanical analysis of FG-CNTRC plates has become subjects of primary interest in recent studies. Shen [11] studied nonlinear bending of simply supported, FG-CNTRC plates in thermal environments. Large amplitude vibration of the CNTRC plates resting on elastic foundation of Pasternak-type has been investigated [12]. Zhu et al. [13] modeled thin-to-moderately thick FG-CNTRC based on the first order shear deformation plate theory and examined bending and free vibration of plates via the finite element method. In another study, compressive and thermal postbuckling of sandwich plates with CNTRC face sheets in thermal environments have been investigated [14]. Bhardwaj et al. [15] analyzed nonlinear flexural and dynamic response of the CNTRC plates by fast converging finite double Chebyshev polynomials. Large deflection analysis of the CNTRC plates has been researched by the element-free kp-Ritz method by Lei et al. [16]. Recently, three-dimensional free vibration of the CNTRC rectangular plates with various boundary conditions has been studied by developing a set of orthogonal admissible functions used in Ritz method [17]. A large deflection geometrically nonlinear behavior of the FG-CNTRC cylindrical panels under uniform point transverse mechanical loading has been studied [18]. In another study, dynamic stability analysis of the FG-CNTRC cylindrical panels under static and periodic axial force by using the mesh-free kp-Ritz method has been investigated [19]. These studies showed that the meshless method is an appropriate technique for modeling the FG-CNTRC structures. A review on the meshless methods for laminated and functionally graded plates and shells can be found in Ref. [20].

In spite of the extensive research in the area of the static and dynamic characteristics of the CNTRC, there has been no attempt to tackle the problem described in the present paper. The aim of this study is to investigate the aeroelastic characteristics of the FG-CNTRC under a supersonic flow. In the present investigation, various distributions of the CNTs in thickness of the CNTRC are considered. Here, the material properties of the CNTRC plates are obtained by a micro-mechanical model. The CNT efficiency parameters are estimated based on matching properties observed from the molecular dynamics simulations and those obtained from the rule of mixture. The equations of motion are developed by Kirchhoff's plate theory and aerodynamic pressure of supersonic flow is modeled by piston theory. To confirm the validity of the present research, the results are compared with those reported in the literature. The influences of volume fraction, aspect ratio and non-dimensional in-plane forces on the stability boundaries of FG-CNTRC plates are also elucidated.

2. Material properties of FG-CNTRC plates

FG-CNTRC plate is a mixture of the CNTs and a polymer matrix. Unlike the isotropic properties of polymer matrix, the CNTs represent anisotropic behavior. The effective material properties of this mixture can be predicted by Mori–Tanaka scheme [21,22] or the rule of mixture [23,24]. Based on the extended rule of mixture, the effective properties of the FG-CNTRCs can be expressed as [11]

$$\begin{aligned} E_{11} &= \eta_1 V_{CNT} E_{11}^{CNT} + V_m E^m \\ \frac{\eta_2}{E_{22}} &= \frac{V_{CNT}}{E_{22}^{CNT}} + \frac{V_m}{E^m} \\ \frac{\eta_3}{G_{12}} &= \frac{V_{CNT}}{G_{12}^{CNT}} + \frac{V_m}{G^m} \end{aligned} \tag{1}$$

where E_{11}^{CNT} and E_{22}^{CNT} represent Young's moduli of the CNTs in directions 1 and 2, respectively, and G_{12}^{CNT} indicates shear modulus of the CNTs. It should be noted that E_{11}, E_{22} and G_{12} are the corresponding properties of the FG-CNTRCs. In addition, E^m and G^m represent Young's modulus and shear modulus of the isotropic polymer matrix. Due to the presence of small scale effect, the CNT efficiency parameters, η_i $(i = 1, 2 \text{ and } 3)$ are introduced in Eq. (1). To calculate the value of the CNT efficiency parameters, elastic modulus of the FG-CNTRCs predicted by the MD simulations should be matched with those determined from the rule of mixture. Moreover, V_{CNT} and V_m are the volume fractions of the CNTs and matrix, respectively and relation among these volume fractions is

$$V_{CNT} + V_m = 1. \tag{2}$$

Similarly, mass density of the FG-CNTRC plates can be expressed as a function of densities of the CNTs and matrix as follows:

$$\rho = V_{CNT}\rho^{CNT} + V_m\rho^m \tag{3}$$

where ρ^{CNT} and ρ^m indicate the densities of CNTs and matrix. In addition, Poisson's ratio can be obtained as

$$\nu_{12} = V_{CNT}^{*}\nu_{12}^{CNT} + (1 - V_{CNT}^{*})\,\nu^m \tag{4}$$

wherein ν_{12}^{CNT} and ν^m are Poisson's ratios of the CNTs and polymer matrix, respectively and V_{CNT}^{*} is defined as follows [25]

$$V_{CNT}^{*} = \frac{w_{CNT}}{w_{CNT} + (\rho^{CNT}/\rho^m)(1 - w_{CNT})} \tag{5}$$

in which w_{CNT} is the mass fraction of the CNTs. Consider a rectangular FG-CNTRC plate of length a in the x direction, width b in the y direction and thickness h in the z direction. CNTs can be distributed either uniformly or functionally graded in the thickness of the FG-CNTRC plates. As shown in Fig. 1, five kinds of distributions of CNTs in the FG-CNTRC plates are studied in this paper. Here, the FG-CNTRC plate with uniform distribution of CNTs is called UD. Moreover, four other types of functionally graded distributions of the CNTs are known as FG-A, FG-V, FG-O and FG-X. The variations of the CNT volume fraction of these five types are defined as follows:

$$\text{UD: } V_{CNT}(z) = V_{CNT}^{*} \tag{6a}$$

$$\text{FG-A: } V_{CNT}(z) = \left(1 - \frac{2z}{h}\right) V_{CNT}^{*} \tag{6b}$$

$$\text{FG-V: } V_{CNT}(z) = \left(1 + \frac{2z}{h}\right) V_{CNT}^{*} \tag{6c}$$

$$\text{FG-O: } V_{CNT}(z) = 2\left(1 - \frac{2\,|z|}{h}\right) V_{CNT}^{*} \tag{6d}$$

$$\text{FG-X: } V_{CNT}(z) = \frac{4\,|z|}{h} V_{CNT}^{*}. \tag{6e}$$

It is noticeable that overall mass fraction of the CNT in different kinds of the FG-CNTRC is equal.

3. Theory and formulations

Based on Kirchhoff's plate theory, the displacements of an arbitrary point of the nanocomposite plate can be expressed as follows:

$$u_x = u(x, y, t) - z\frac{\partial w}{\partial x} \qquad u_y = v(x, y, t) - z\frac{\partial w}{\partial y} \qquad u_z = w(x, y, t) \tag{7}$$

where u, v and w indicate displacement of the point $(x, y, 0)$ along x, y and z directions, respectively. Using von-Karman strains, the strain–displacement relations are expressed as

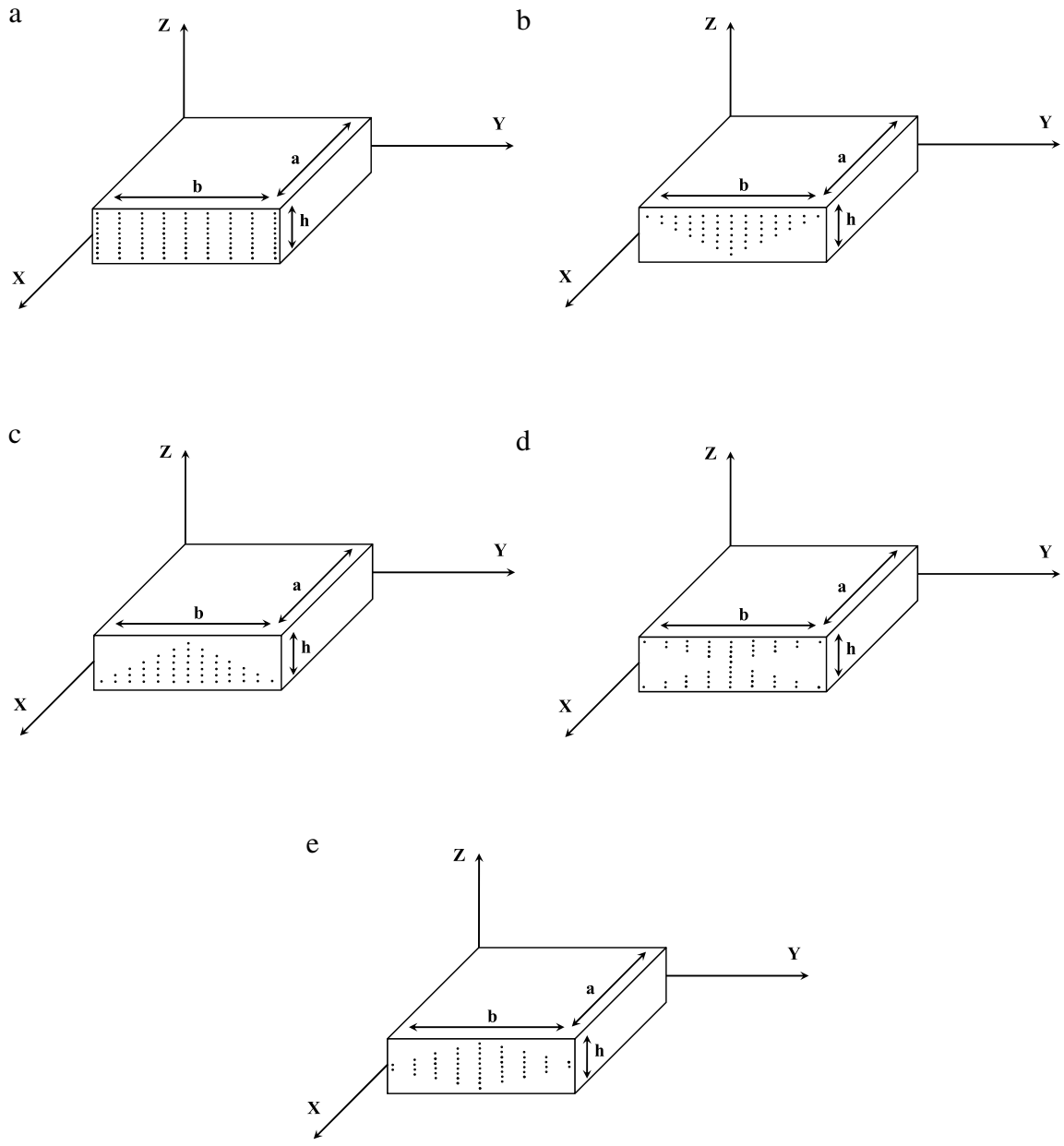

Fig. 1. Configurations of the FG-CNTRC plates (a) UD; (b) FG-V; (c) FG-A; (d) FG-X; (e) FG-O.

$$\varepsilon_{xx} = \frac{\partial u}{\partial x} - z\frac{\partial^2 w}{\partial x^2} + \frac{1}{2}\left(\frac{\partial w}{\partial x}\right)^2 \qquad \varepsilon_{yy} = \frac{\partial v}{\partial y} - z\frac{\partial^2 w}{\partial y^2} + \frac{1}{2}\left(\frac{\partial w}{\partial y}\right)^2$$
$$\varepsilon_{xy} = \frac{1}{2}\left(\frac{\partial u}{\partial y} + \frac{\partial v}{\partial x} - 2z\frac{\partial^2 w}{\partial y \partial x} + \frac{\partial w}{\partial x}\frac{\partial w}{\partial y}\right). \tag{8}$$

Due to orthotropic characteristics of the CNTs, the mechanical constitutive relations of the FG-CNTRC plates are defined as

$$\begin{pmatrix}\sigma_{xx}\\ \sigma_{yy}\\ \sigma_{xy}\end{pmatrix}=\begin{bmatrix}\dfrac{E_{11}}{1-\nu_{12}\nu_{21}} & \dfrac{\nu_{12}E_{22}}{1-\nu_{12}\nu_{21}} & 0\\ \dfrac{\nu_{12}E_{22}}{1-\nu_{12}\nu_{21}} & \dfrac{E_{22}}{1-\nu_{12}\nu_{21}} & 0\\ 0 & 0 & G_{12}\end{bmatrix}\begin{pmatrix}\varepsilon_{xx}\\ \varepsilon_{yy}\\ 2\varepsilon_{xy}\end{pmatrix}. \tag{9}$$

Applying Hamilton's principle, the following governing equations can be obtained:

$$\frac{\partial N_{xx}}{\partial x}+\frac{\partial N_{xy}}{\partial y}=I_0\frac{\partial^2 u}{\partial t^2}-I_1\frac{\partial^3 w}{\partial x\,\partial t^2} \tag{10a}$$

$$\frac{\partial N_{xy}}{\partial x}+\frac{\partial N_{yy}}{\partial y}=I_0\frac{\partial^2 v}{\partial t^2}-I_1\frac{\partial^3 w}{\partial y\,\partial t^2} \tag{10b}$$

$$\begin{aligned}&\frac{\partial^2 M_{xx}}{\partial x^2}+\frac{\partial^2 M_{yy}}{\partial y^2}+2\frac{\partial^2 M_{xy}}{\partial x\partial y}+N_{xx}\frac{\partial^2 w}{\partial x^2}+N_{yy}\frac{\partial^2 w}{\partial y^2}\\ &\quad+2N_{xy}\frac{\partial^2 w}{\partial x\partial y}=\Delta p+I_0\frac{\partial^2 w}{\partial t^2}+I_1\left(\frac{\partial^3 u}{\partial x\,\partial t^2}+\frac{\partial^3 v}{\partial y\,\partial t^2}\right)-I_2\left(\frac{\partial^4 w}{\partial x^2\partial t^2}+\frac{\partial^4 w}{\partial y^2\partial t^2}\right)\end{aligned} \tag{10c}$$

wherein q is the distributed transverse load on the FG-CNTRC plate. Also, I_0, I_1 and I_2 are the normal, coupled normal-rotary and rotary inertial coefficients, respectively, and are defined by

$$I_0=\int_{-h/2}^{h/2}\rho\,dz\qquad I_1=\int_{-h/2}^{h/2}\rho\,z\,dz\qquad I_2=\int_{-h/2}^{h/2}\rho\,z^2dz. \tag{11}$$

In addition, N_{xx}, N_{yy} and N_{xy} denote in-face stress resultants and M_{xx}, M_{yy} and M_{xy} are stress couple resultants defined as

$$\{N_{xx},N_{yy},N_{xy},M_{xx},M_{yy},M_{xy}\}=\int_{-\frac{h}{2}}^{\frac{h}{2}}\{\sigma_{xx},\sigma_{yy},\sigma_{xy},\sigma_{xx}z,\sigma_{yy}z,\sigma_{xy}z\}dz. \tag{12}$$

One can obtain in-face stress resultants and stress couple resultants as functions of displacements by employing strain–displacement relationships (Eq. (8)), stress–strain relationships (Eq. (9)) and stress resultants definition (Eq. (12)). Substituting stress resultants into governing equations and ignoring nonlinear terms lead to the governing differential equations in terms of the transverse and in-plane displacements, i.e.,

$$A_1\frac{\partial^2 u}{\partial x^2}+C_1\frac{\partial^2 u}{\partial y^2}+(\nu_{12}B_1+C_1)\frac{\partial^2 v}{\partial x\partial y}-A_2\frac{\partial^3 w}{\partial x^3}-(\nu_{12}B_2+2C_2)\frac{\partial^3 w}{\partial x\partial y^2}=I_0\frac{\partial^2 u}{\partial t^2}-I_1\frac{\partial^3 w}{\partial x\,\partial t^2} \tag{13a}$$

$$C_1\frac{\partial^2 v}{\partial x^2}+B_1\frac{\partial^2 v}{\partial y^2}+(\nu_{12}B_1+C_1)\frac{\partial^2 u}{\partial x\partial y}-B_2\frac{\partial^3 w}{\partial y^3}-(\nu_{12}B_2+2C_2)\frac{\partial^3 w}{\partial x^2\partial y}=I_0\frac{\partial^2 v}{\partial t^2}-I_1\frac{\partial^3 w}{\partial y\,\partial t^2} \tag{13b}$$

$$\begin{aligned}&A_3\frac{\partial^4 w}{\partial x^4}+2(\nu_{12}B_3+2C_3)\frac{\partial^4 w}{\partial x^2\partial y^2}+B_3\frac{\partial^4 w}{\partial y^4}-A_2\frac{\partial^3 u}{\partial x^3}-B_2\frac{\partial^3 v}{\partial y^3}-(\nu_{12}B_2+2C_2)\left(\frac{\partial^3 u}{\partial x\partial y^2}+\frac{\partial^3 v}{\partial x^2\partial y}\right)\\ &\quad=\Delta p+N_{xx}\frac{\partial^2 w}{\partial x^2}+N_{yy}\frac{\partial^2 w}{\partial y^2}+2N_{xy}\frac{\partial^2 w}{\partial x\partial y}-I_0\frac{\partial^2 w}{\partial t^2}-I_1\left(\frac{\partial^3 u}{\partial x\partial t^2}+\frac{\partial^3 v}{\partial y\partial t^2}\right)\\ &\qquad+I_2\left(\frac{\partial^4 w}{\partial x^2\partial t^2}+\frac{\partial^4 w}{\partial y^2\partial t^2}\right)\end{aligned} \tag{13c}$$

where A_i, B_i and C_i $(i = 1, 2, 3)$ are defined by

$$\begin{Bmatrix} A_1 \\ A_2 \\ A_3 \end{Bmatrix} = \int_{-\frac{h}{2}}^{\frac{h}{2}} \left(\frac{E_{11}}{(1-\nu_{12}\nu_{21})} \right) \begin{Bmatrix} 1 \\ z \\ z^2 \end{Bmatrix} dz \qquad \begin{Bmatrix} B_1 \\ B_2 \\ B_3 \end{Bmatrix} = \int_{-\frac{h}{2}}^{\frac{h}{2}} \left(\frac{E_{22}}{(1-\nu_{12}\nu_{21})} \right) \begin{Bmatrix} 1 \\ z \\ z^2 \end{Bmatrix} dz$$
$$\begin{Bmatrix} C_1 \\ C_2 \\ C_3 \end{Bmatrix} = \int_{-\frac{h}{2}}^{\frac{h}{2}} G_{12} \begin{Bmatrix} 1 \\ z \\ z^2 \end{Bmatrix} dz. \tag{14}$$

It is noticed that the governing differential equations are coupled. From Eq. (13c), it is easily seen that the traditional classical plate theory is recovered if the parameters A_2, B_2, C_2 and I_1 are set to zero. Here, it is assumed that the FG-CNTRC plate is subjected to external fluid flow passing over the top surface of the plate. To evaluate the aerodynamic pressure of supersonic flow, piston theory is utilized as [26]:

$$\Delta p = \frac{\rho_\infty U_\infty^2}{\sqrt{M_\infty^2 - 1}} \left[\frac{\partial w}{\partial x} + \left(\frac{1}{U_\infty} \right) \frac{M_\infty^2 - 2}{M_\infty^2 - 1} \frac{\partial w}{\partial t} \right] \tag{15}$$

where Δp is the aerodynamic pressure and U_∞, ρ_∞ and M_∞ indicate free stream velocity, air density and Mach number, respectively. The term "piston theory", as used in this paper, refers to a method for calculating the aerodynamic loads on the structures in which the local pressure generated by the structure's motion is related to the local normal component of fluid velocity in the same way that these quantities are related at the face of a piston moving in a one-dimensional channel. The piston theory may be employed for large Mach Numbers or high reduced frequencies of unsteady motion, whenever the surface involved is nearly plane and not inclined too sharply to the direction of the free stream [27]. It has been shown that for Mach number greater than 1.6, the results based on the two-dimensional static aerodynamic theory approximation are in good agreement with those obtained from the exact aerodynamic theory. In addition, for even lower Mach numbers and aspect ratios between 2 and 6, complete agreement has been confirmed [28,29]. Based on this static approximation, the aerodynamic pressure is expressed as

$$\Delta p = \frac{\rho_\infty U_\infty^2}{\sqrt{M_\infty^2 - 1}} \frac{\partial w}{\partial x}. \tag{16}$$

Applying the approximate aerodynamic pressure, the governing equations are obtained as

$$A_1 \frac{\partial^2 u}{\partial x^2} + C_1 \frac{\partial^2 u}{\partial y^2} + (\nu_{12} B_1 + C_1) \frac{\partial^2 v}{\partial x \partial y} - A_2 \frac{\partial^3 w}{\partial x^3} - (\nu_{12} B_2 + 2C_2) \frac{\partial^3 w}{\partial x \partial y^2} = I_0 \frac{\partial^2 u}{\partial t^2} - I_1 \frac{\partial^3 w}{\partial x\, \partial t^2} \tag{17a}$$

$$C_1 \frac{\partial^2 v}{\partial x^2} + B_1 \frac{\partial^2 v}{\partial y^2} + (\nu_{12} B_1 + C_1) \frac{\partial^2 u}{\partial x \partial y} - B_2 \frac{\partial^3 w}{\partial y^3} - (\nu_{12} B_2 + 2C_2) \frac{\partial^3 w}{\partial x^2 \partial y} = I_0 \frac{\partial^2 v}{\partial t^2} - I_1 \frac{\partial^3 w}{\partial y\, \partial t^2} \tag{17b}$$

$$\begin{aligned} &A_3 \frac{\partial^4 w}{\partial x^4} + 2(\nu_{12} B_3 + 2C_3) \frac{\partial^4 w}{\partial x^2 \partial y^2} + B_3 \frac{\partial^4 w}{\partial y^4} - A_2 \frac{\partial^3 u}{\partial x^3} - B_2 \frac{\partial^3 v}{\partial y^3} \\ &\quad - (\nu_{12} B_2 + 2C_2) \left(\frac{\partial^3 u}{\partial x \partial y^2} + \frac{\partial^3 v}{\partial x^2 \partial y} \right) + \frac{\rho_\infty U_\infty^2}{\sqrt{M_\infty^2 - 1}} \frac{\partial w}{\partial x} = N_{xx} \frac{\partial^2 w}{\partial x^2} + N_{yy} \frac{\partial^2 w}{\partial y^2} \\ &\quad + 2N_{xy} \frac{\partial^2 w}{\partial x \partial y} - I_0 \frac{\partial^2 w}{\partial t^2} - I_1 \left(\frac{\partial^3 u}{\partial x \partial t^2} + \frac{\partial^3 v}{\partial y \partial t^2} \right) + I_2 \left(\frac{\partial^4 w}{\partial x^2 \partial t^2} + \frac{\partial^4 w}{\partial y^2 \partial t^2} \right). \end{aligned} \tag{17c}$$

In this study, to present a realistic model, the viscoelastic property of the FG-CNTRC plates and the aerodynamic damping are considered by taking into account the total damping coefficient. The total damping coefficient, G_T, is derived based on summation of aerodynamic damping coefficient, G_A [30], and effective structural damping coefficient, G_S. The aerodynamic damping coefficient can be expressed as

$$G_A = \frac{\rho_\infty U_\infty}{\sqrt{M_\infty^2 - 1}} \frac{M_\infty^2 - 2}{M_\infty^2 - 1}. \tag{18}$$

Due to this assumption, third governing equation (Eq. (17c)) is modified as follows:

$$
\begin{aligned}
&A_3\frac{\partial^4 w}{\partial x^4}+2(\nu_{12}B_3+2C_3)\frac{\partial^4 w}{\partial x^2\partial y^2}+B_3\frac{\partial^4 w}{\partial y^4}-A_2\frac{\partial^3 u}{\partial x^3}-B_2\frac{\partial^3 v}{\partial y^3}\\
&\quad-(\nu_{12}B_2+2C_2)\left(\frac{\partial^3 u}{\partial x\partial y^2}+\frac{\partial^3 v}{\partial x^2\partial y}\right)+\frac{\rho_\infty U_\infty^2}{\sqrt{M_\infty^2-1}}\frac{\partial w}{\partial x}\\
&=-G_T\frac{\partial w}{\partial t}+N_{xx}\frac{\partial^2 w}{\partial x^2}+N_{yy}\frac{\partial^2 w}{\partial y^2}+2N_{xy}\frac{\partial^2 w}{\partial x\partial y}-I_0\frac{\partial^2 w}{\partial t^2}-I_1\left(\frac{\partial^3 u}{\partial x\partial t^2}+\frac{\partial^3 v}{\partial y\partial t^2}\right)\\
&\quad+I_2\left(\frac{\partial^4 w}{\partial x^2\partial t^2}+\frac{\partial^4 w}{\partial y^2\partial t^2}\right).
\end{aligned}
\tag{19}
$$

Up to now, the analysis has been general without reference to the boundary conditions. The boundary conditions can be set in a number of ways depending on what particular physical models are used for the simulation. In this study, two experimentally interesting boundary conditions such as four edges fully clamped (CCCC) and four edges immovable simply supported (SSSS) boundary conditions are considered. In addition, to simplify the analysis, the following non-dimensional parameters are defined:

$$
\begin{aligned}
&X=\frac{x}{a}\qquad Y=\frac{y}{b}\qquad H=\frac{h}{a}\qquad \lambda=\frac{\rho_\infty U_\infty^2 a^3}{A_3\sqrt{M_\infty^2-1}}\\
&r_{xx}=-\frac{N_{xx}a^2}{A_3}\qquad r_{yy}=-\frac{N_{yy}a^2}{A_3}\qquad r_{xy}=-\frac{N_{xy}a^2}{A_3}\qquad \tau=t\frac{h}{a^2}\sqrt{\frac{E^m}{\rho^m}}\\
&r=\frac{a}{b}\qquad g_T=g_A+g_S\qquad g_S=G_S\sqrt{\frac{E^m}{\rho^m}}\frac{Ha^3}{A_3\pi^4}\qquad g_A=\lambda\sqrt{\frac{E^m}{\rho^m}}\frac{M_\infty^2-2}{M_\infty^2-1}\frac{H}{U_\infty\pi^4}.
\end{aligned}
\tag{20}
$$

Substituting Eq. (20) into the governing equations, the non-dimensional governing equations are developed, i.e.,

$$
\begin{aligned}
&\frac{\partial^2 u}{\partial X^2}+\frac{C_1}{A_1}r^2\frac{\partial^2 u}{\partial Y^2}+\left(\frac{\nu_{12}B_1+C_1}{A_1}\right)r\frac{\partial^2 v}{\partial X\partial Y}-\frac{A_2}{A_1 a}\frac{\partial^3 w}{\partial X^3}-\left(\frac{\nu_{12}B_2+2C_2}{A_1 a}\right)r^2\frac{\partial^3 w}{\partial X\partial Y^2}\\
&\quad=H^2\left(\frac{I_0E^m}{\rho^m A_1}\right)\frac{\partial^2 u}{\partial\tau^2}-H^2\left(\frac{I_1E^m}{a\rho^m A_1}\right)\frac{\partial^3 w}{\partial X\,\partial\tau^2}
\end{aligned}
\tag{21a}
$$

$$
\begin{aligned}
&\frac{\partial^2 v}{\partial Y^2}+\frac{C_1}{B_1r^2}\frac{\partial^2 v}{\partial X^2}+\left(\frac{\nu_{12}B_1+C_1}{B_1 r}\right)\frac{\partial^2 u}{\partial X\partial Y}-\frac{B_2 r}{B_1 a}\frac{\partial^3 w}{\partial Y^3}-\left(\frac{\nu_{12}B_2+2C_2}{B_1 ar}\right)\frac{\partial^3 w}{\partial X^2\partial Y}\\
&\quad=\frac{H^2}{r^2}\left(\frac{I_0E^m}{\rho^m B_1}\right)\frac{\partial^2 v}{\partial\tau^2}-\frac{H^2}{r}\left(\frac{I_1E^m}{\rho^m B_1 a}\right)\frac{\partial^3 w}{\partial Y\,\partial\tau^2}
\end{aligned}
\tag{21b}
$$

$$
\begin{aligned}
&\frac{\partial^4 w}{\partial X^4}+2\left(\frac{\nu_{12}B_3+2C_3}{A_3}\right)r^2\frac{\partial^4 w}{\partial X^2\partial Y^2}+\frac{B_3}{A_3}r^4\frac{\partial^4 w}{\partial Y^4}-a\left(\frac{\nu_{12}B_2+2C_2}{A_3}\right)\\
&\quad\times\left(r^2\frac{\partial^3 u}{\partial X\partial Y^2}+r\frac{\partial^3 v}{\partial X^2\partial Y}\right)-\frac{A_2 a}{A_3}\frac{\partial^3 u}{\partial X^3}-\frac{B_2 a}{A_3}r^3\frac{\partial^3 v}{\partial Y^3}\\
&=-\pi^4 g_T\frac{\partial w}{\partial\tau}-\lambda\frac{\partial w}{\partial X}+r_{xx}\frac{\partial^2 w}{\partial X^2}+r^2 r_{yy}\frac{\partial^2 w}{\partial Y^2}+2rr_{xy}\frac{\partial^2 w}{\partial X\partial Y}-H^2\left(\frac{I_0E^m a^2}{\rho^m A_3}\right)\frac{\partial^2 w}{\partial\tau^2}\\
&\quad-H^2\left(\frac{I_1E^m a}{\rho^m A_3}\right)\left(\frac{\partial^3 u}{\partial X\partial\tau^2}+r\frac{\partial^3 v}{\partial Y\partial\tau^2}\right)+H^2\left(\frac{I_2E^m}{\rho^m A_3}\right)\left(\frac{\partial^4 w}{\partial X^2\partial\tau^2}+r^2\frac{\partial^4 w}{\partial Y^2\partial\tau^2}\right).
\end{aligned}
\tag{21c}
$$

4. Solution procedure

It is difficult to achieve the exact solution, as a result of complexity and coupling of the governing differential equations. Hence, Galerkin's method is applied to obtain the solution in a general way. Using Galerkin's method, partial differential equations are converted into a set of ordinary differential equations. Therefore, the following displacements are assumed to approximate the aeroelastic characteristics of the system [31]:

$$\begin{aligned} u(X, Y, \tau) &= \mathbf{\Phi}_u^T \mathbf{q}_u \\ v(X, Y, \tau) &= \mathbf{\Phi}_v^T \mathbf{q}_v \\ w(X, Y, \tau) &= \mathbf{\Phi}_w^T \mathbf{q}_w \end{aligned} \tag{22}$$

where $\mathbf{q}_u$, $\mathbf{q}_v$ and $\mathbf{q}_w$ are time dependent vectors of generalized coordinates, and $\mathbf{\Phi}_u$, $\mathbf{\Phi}_v$ and $\mathbf{\Phi}_w$ are shape functions. Substituting approximate displacement expressions (Eq. (22)) into Eq. (21), multiplying both sides of the equations by shape functions and integrating over the whole region, the discretized expressions for the equations of motion can be obtained. Due to the convenient and compact form of state space, the set of ordinary differential equations is derived in the state space form as follows:

$$\dot{\mathbf{q}} = \mathbf{A}^{-1}\mathbf{B}\ \mathbf{q} \tag{23}$$

where matrix $\mathbf{A}$ represents dynamic coupling of the transverse and in-plane displacements. Moreover, matrix $\mathbf{B}$ indicates static coupling of generalized coordinates and includes stiffness terms of the system and aeroelastic effect of supersonic air flow. Components of the above matrices are given in the Appendix. Furthermore, $\mathbf{q}$ is the overall vector of generalized coordinates i.e.,

$$\{\mathbf{q}\} = \left\{ \mathbf{q}_{u1}^T\ \mathbf{q}_{u2}^T\ \mathbf{q}_{v1}^T\ \mathbf{q}_{v2}^T\ \mathbf{q}_{w1}^T\ \mathbf{q}_{w2}^T \right\}^T \tag{24}$$

where

$$\begin{aligned} &\mathbf{q}_{u1} = \mathbf{q}_u \qquad \mathbf{q}_{v1} = \mathbf{q}_v \qquad \mathbf{q}_{w1} = \mathbf{q}_w \\ &\mathbf{q}_{u2} = \dot{\mathbf{q}}_{u1} \qquad \mathbf{q}_{v2} = \dot{\mathbf{q}}_{v1} \qquad \mathbf{q}_{w2} = \dot{\mathbf{q}}_{w1}. \end{aligned} \tag{25}$$

By solving the eigenvalue problem of Eq. (23), the stability boundaries of the FG-CNTRC plate can be computed.

5. Numerical results and discussion

To verify the accuracy of present formulation, the results of this study are compared against available results in the literature for three cases. First of all, stability boundaries of an isotropic plate are determined and compared with those reported by Dugundji [32]. Dugundji assumed that rectangular panel is simply supported on all four edges and has a structural damping. Here, it is assumed that the aspect ratio is equal to 2 and non-dimensional in-plane force in y direction, r_{yy}, is equal to zero. The stability boundaries for various values of non-dimensional total damping coefficient are displayed in Fig. 2. The results are found to be in good agreement with the existing data in Ref. [32].

In second case, to clarify the accuracy of the current solution in the presence of volume fraction exponent, non-dimensional frequencies of Al–ZrO_2 FGM plates with movable simply supported boundary condition are considered. In this case, we take $E_m = 68.9$ GPa, $\rho_m = 2700\ \mathrm{kg/m^3}$ for Al and $E_c = 211$ GPa, $\rho_c = 4500\ \mathrm{kg/m^3}$ for ZrO_2 [33]. Also, Poisson's ratio, υ, is set to 0.33 for both Al and ZrO_2 and length to thickness ratio is equal to 100. The non-dimensional frequencies ($\tilde{\omega}_{mn} = \omega_{mn}\left(a^2/h\right)\sqrt{\rho_c/E_c}$) for various volume fraction exponents, k, are listed in Table 1. It is seen that the present results are in good agreement with the previous results [33].

In third case, non-dimensional frequencies of the FG-CNTRC square plates in various distributions of the CNTs are compared with those reported by Zhu et al. [13]. Properties of carbon nanotube and matrix are assumed the same as mentioned in Ref. [13]. Also, it is assumed that all edges of plates are movable simply supported and length to thickness ratio is equal to 50. The results of comparison study are listed in Table 2 and reveal that despite applying different theory, the suggested model is justified by a good agreement between the results given by present model and the results reported in Ref. [13]. In final validation case, non-dimensional frequencies ($=\omega(ab/h)\sqrt{\rho^m/E^m}$)

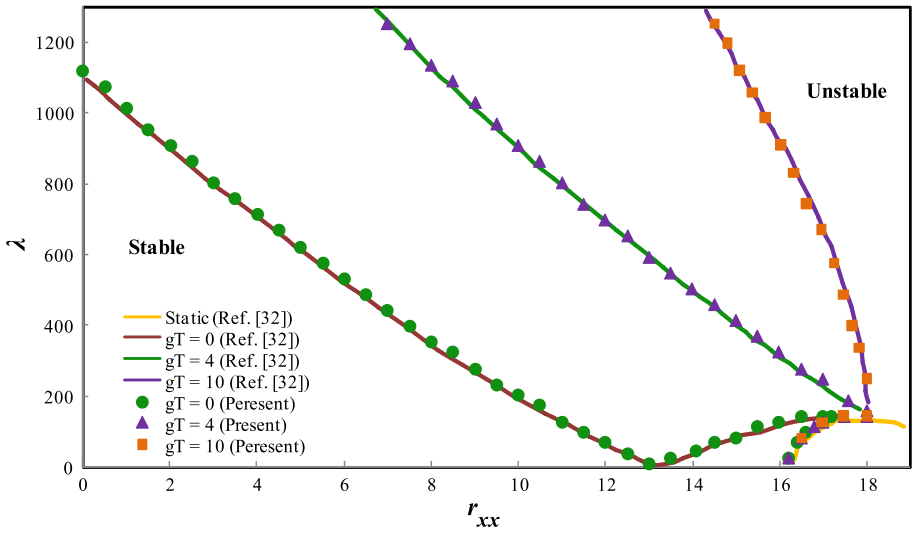

Fig. 2. Comparison between the results of present model and those given by Dugundji [32] for stability boundaries of isotropic plate for different values of non-dimensional total damping coefficient.

Table 1
Validation of non-dimensional frequencies of Al–ZrO_2 FGM plates.

Aspect ratio (a/b)		Volume fraction exponents			
		$k = 0$	$k = 1$	$k = 10$	$k = 100$
1	Ref. [33]	5.9713	5.1190	4.6765	4.3470
	Present	6.0359	5.2545	5.0090	4.5645
$1/\sqrt{2}$	Ref. [33]	4.4788	3.8396	3.5077	3.2605
	Present	4.5270	3.9410	3.7569	3.4234

of the clamped UD CNTRC plates with different values of aspect ratio are depicted in Fig. 3 and compared with those reported by Abdollahzadeh Shahrbabaki and Alibeigloo [17] based on three-dimensional elasticity. Properties of carbon nanotube and matrix are also assumed the same as mentioned in Ref. [13]. In addition, the length to thickness ratio is equal to 50 and $V^*_{CNT} = 0.11$. Reasonable agreement between the present results and reported results in Ref. [17] is seen. After verifying the accuracy and reliability of the present formulation, we now proceed to the application of this method to various cases.

To show the aeroelastic characteristics of FG-CNTRC plates, parametric studies are carried out. The FG-CNTRC plates are made of carbon nanotubes embedded into polymer matrix. Here, polymethyl methacrylate, well-known as PMMA, is considered as matrix material. Mechanical properties of PMMA are assumed to be $E^m = 2.5$ GPa, $\nu^m = 0.34$ and $\rho^m = 1150$ kg/m^3. For numerical results, (10, 10) SWCNTs are chosen as reinforcements and the following properties are considered [13]:

$$E_{11}^{CNT} = 5.6466 \text{ TPa}, \qquad E_{22}^{CNT} = 7.0800 \text{ TPa}, \qquad G_{12}^{CNT} = 1.9445 \text{ TPa},$$
$$\nu_{12}^{CNT} = \nu_{21}^{CNT} = 0.175 \quad \text{and} \quad \rho^{CNT} = 1400 \text{ kg/m}^3.$$

Han and Elliott [10] explained that the general macroscopic rule of mixtures cannot be applied directly to nanocomposites and this method should be modified. Therefore, to modify the rule of mixtures, the CNT efficiency parameters are estimated based on matching properties predicted by the MD simulations and those obtained from the rule of mixture. The values of the CNT efficiency parameters for different volume fractions are listed in Table 3 [10,11]. These values will be used in all of the following parametric studies.

To show the effect of boundary condition, the stability boundaries of immovable simply supported and clamped supported plates subject to aerodynamic load are studied. The stability boundaries of the FG-UD plate for two values

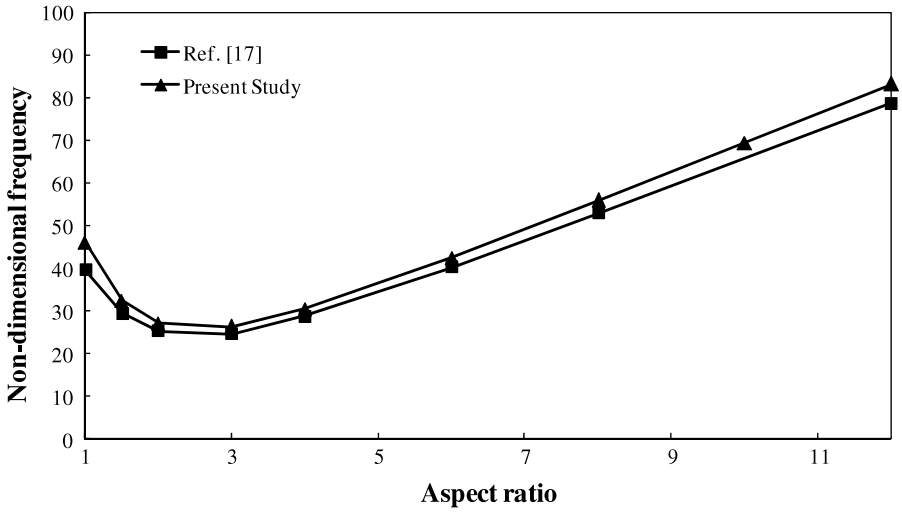

Fig. 3. Comparison between the results of present model and those given by Abdollahzadeh Shahrbabaki and Alibeigloo [17].

Table 2
Comparison of non-dimensional frequencies of the FG-CNTRC square plates for various distributions of the CNTs.

	V^*_{CNT}	Ref. [13]	Present study
	0.11	19.223	20.616
UD	0.14	21.354	23.026
	0.17	23.697	25.304
	0.11	16.252	17.277
FG-V	0.14	17.995	19.208
	0.17	19.982	21.151
	0.11	22.984	24.923
FG-X	0.14	25.555	27.916
	0.17	28.413	30.658
	0.11	14.302	15.139
FG-O	0.14	15.801	16.783
	0.17	17.544	18.497

Table 3
CNT efficiency parameters for various volume fractions.

V^*_{CNT}	η_1	η_2	η_3
0.12	0.137	1.022	0.715
0.17	0.142	1.626	1.138
0.28	0.141	1.585	1.109

of non-dimensional total damping coefficient are displayed in Fig. 4. In this figure, we take $r = 2, r_{xy} = 0, r_{yy} = 0$, $H = 0.01$ and $V^*_{CNT} = 0.12$. It can be seen that the stable region of plate with four edges simply supported is smaller than that of plate with four edges clamped because clamped boundary condition yields an increase of stiffness of the plate and the FG-CNTRC plate becomes stiffer.

To illustrate the effect of the aspect ratio, the critical aerodynamic pressure is displayed in Fig. 5 for different distributions of the CNTs. In this figure, we take $g_T = 0, r_{xx} = 0, r_{xy} = 0, r_{yy} = 0, H = 0.01$ and $V^*_{CNT} = 0.12$. It is clear that the critical aerodynamic pressure increases with an increase in aspect ratio. In another word, the stable region can be extended by increasing the aspect ratio. The results are actually in good agreement with the previous works

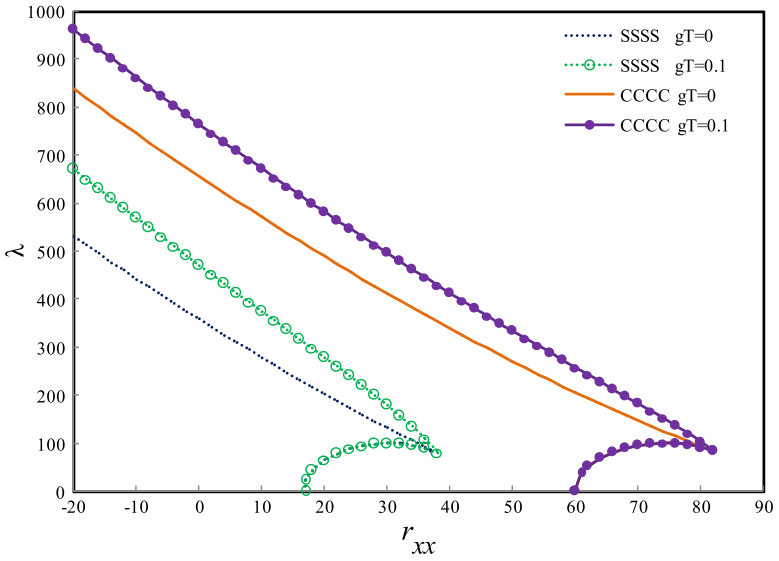

Fig. 4. Effect of boundary condition on the aeroelastic stability of UD plates.

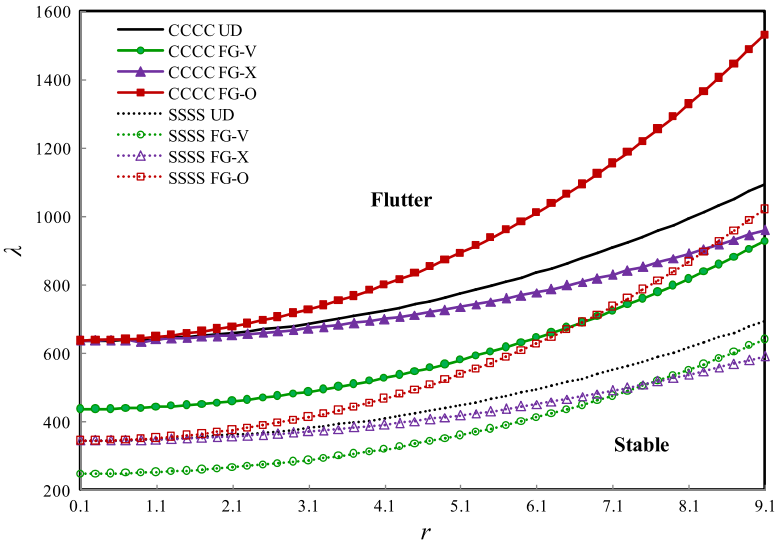

Fig. 5. Variation of critical aerodynamic pressure with the aspect ratio for different FG-CNTRC plates ($V^*_{CNT} = 0.12$).

[1,5]. It is also seen that the FG-O plate has the greatest stable region in comparison with other plates. Moreover, based on the numerical calculations, the results reveal that FG-A and FG-V plates have the same aeroelastic characteristics. Therefore, in this figure and the following numerical results, the results of the FG-V plate are only represented.

Fig. 6(a) and (b) demonstrate the variations of the critical aerodynamic pressure as a function of non-dimensional in-plane forces in x- and y-directions, respectively. In Fig. 6(a), the parameters are fixed at $g_T = 0$, $r_{xy} = 0$, $r_{yy} = 0$, $r = 1$ and $V^*_{CNT} = 0.12$. It can be seen that with the increase of non-dimensional in-plane force in x direction, the critical aerodynamic pressure decreases. Therefore, the FG-CNTRC plate begins to oscillate with a self-excited harmonic motion at smaller speeds. It physically means that the compressive in-plane force in x direction decreases the stiffness of the plate, which results in a lower critical freestream pressure than an unstressed plate. Moreover, at specific value of r_{xx}, the critical aerodynamic pressures for all FG-CNTRC plates except FG-V plate are approximately identical. Also, the critical dynamic pressures of the FG-V plate are lower than the critical dynamic

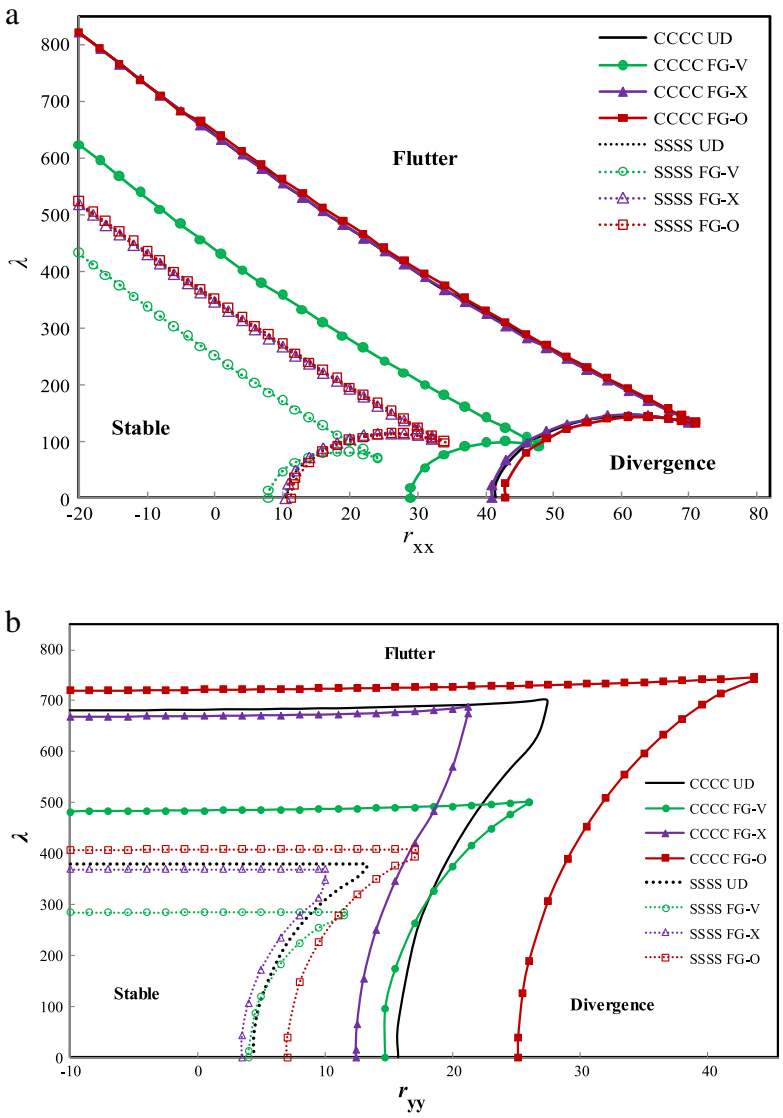

Fig. 6. Effect of non-dimensional in-plane forces on the aeroelastic stability of various FG-CNTRC plates; (a) Non-dimensional in-plane force in x-direction and (b) Non-dimensional in-plane force in y-direction.

pressures of other plates. Although it is not shown here, by applying various V^*_{CNT}, the stability boundaries of all FG-CNTRCs do not have noticeable changes.

The effect of non-dimensional in-plane force in y direction, r_{yy}, on the aeroelastic characteristics of the FG-CNTRC is illustrated in Fig. 6(b). The parameters needed for numerical calculation in this figure are assumed to be $g_T = 0$, $r_{xy} = 0$, $r_{xx} = 0$, $r = 3$, $H = 0.01$ and $V^*_{CNT} = 0.12$. Unlike the non-dimensional in-plane force in x direction, the presence of non-dimensional in-plane force in y direction does not affect dynamic stability boundaries and dynamic unstable region remains unchanged. Similar to r_{xx}, applying r_{yy} can be caused divergence instability. As observed, FG-O plate has the greatest stable region with respect to other plates. Also, FG-X has the greatest static unstable region and FG-V has the greatest dynamic unstable region. The influence of the various V^*_{CNT} on the FG-O square plate is plotted in Fig. 7. It is seen that by applying various V^*_{CNT}, static stability boundaries vary and dynamic stability boundaries remain unchanged. It is observed that FG-O plate with $V^*_{CNT} = 0.17$ has the greatest stable region with respect to other values of V^*_{CNT}.

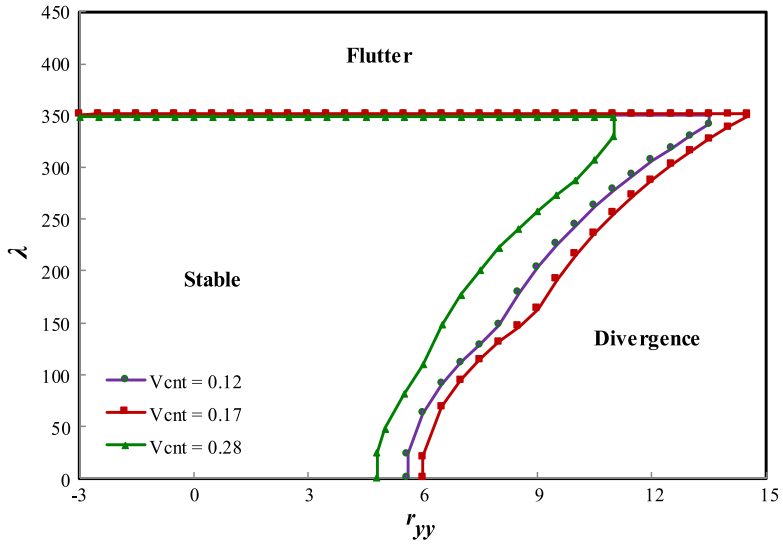

Fig. 7. Variation of the critical aerodynamic pressure of FG-O plate with respect to r_{yy} for three values of V^*_{CNT}.

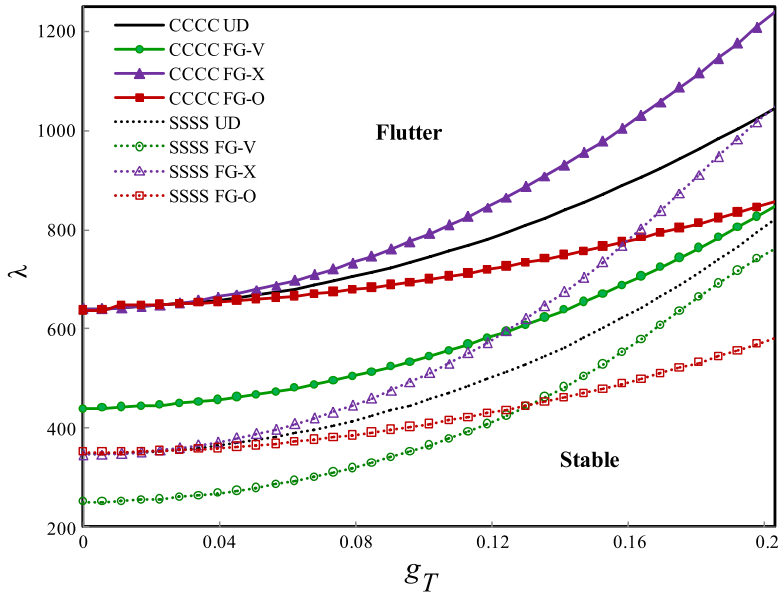

Fig. 8. Variation of stability boundaries with respect to total damping coefficient for various kinds of FG-CNTRC plates.

Fig. 8 shows aeroelastic characteristic of the FG-CNTRC plates in the presence of non-dimensional total damping coefficient, g_T. Here, we take $r_{xx} = 0$, $r_{xy} = 0$, $r_{yy} = 0$, $r = 1$, $H = 0.01$ and $V^*_{CNT} = 0.12$. It should be noted that with the increase of g_T, the critical aerodynamic pressure increases. These results reveal that the damping appreciably improves the flutter boundaries and so it can be concluded that the damping could stabilize the flutter boundaries of systems. Numerical analysis demonstrates that the FG-X plate has the greatest stable region.

As a final numerical example, Fig. 9 represents the variation of the stability boundaries of the FG-X plate with respect to total damping for various V^*_{CNT}. The results show that by increasing V^*_{CNT}, the critical aerodynamic pressure increases. This is to be expected, because the increase of the carbon nanotube volume fraction yields an increase of stiffness of the plate and the FG-CNTRC plate becomes stiffer.

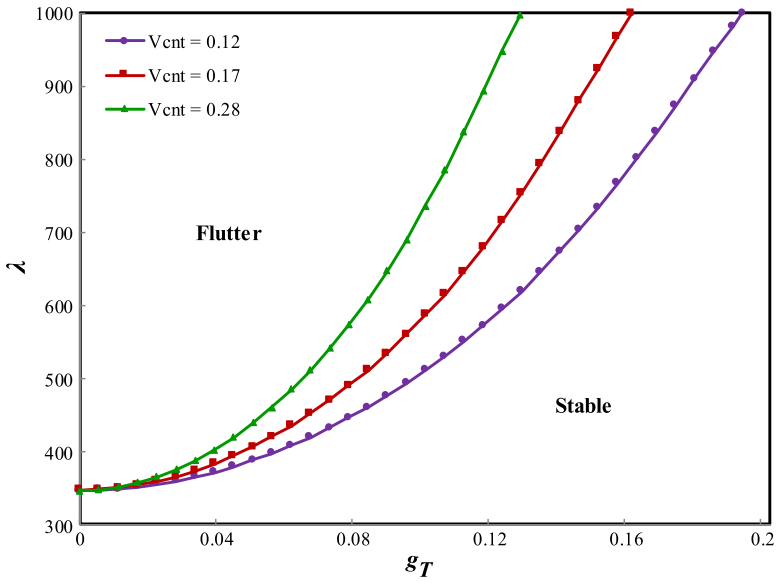

Fig. 9. Effect of V^*_{CNT} on the variation of λ with respect to total damping coefficient.

6. Conclusion

We have presented the first attempt to predict the aeroelastic characteristics of the FG-CNTRC plates under the supersonic flow. In spite of some achievement in vibration analysis of the FG-CNTRC plates, to the authors' knowledge, there has been no attempt to tackle the problem described in the present investigation. Evaluation of the aeroelastic characteristics of FG-CNTRC plates is the main contribution of the present paper. In this work, on the basis of the rule of mixture, the effective properties of the FG-CNTRC plates were obtained. The governing equations of motion were derived by utilizing Kirchhoff's plate theory and Hamilton's principle. Since the FG-CNTRC plate is subjected to supersonic flow, the first order piston theory was applied. The critical aerodynamic pressure was obtained for five types of FG-CNTRC plates. The obtained results have been successfully compared to existing data in the literature. To study the aeroelastic behavior, the effects of aspect ratio, non-dimensional in-plane forces and non-dimensional total damping coefficient on the stability boundaries were examined. Based on the numerical results, it was found that with the increase of aspect ratio and total damping, the critical aerodynamic pressure increases. Moreover, it was observed that by increasing the non-dimensional in-plane force in x direction, the critical aerodynamic pressure decreases whereas applying r_{yy} does not affect dynamic stable region. Furthermore, it was revealed that FG-A and FG-V plates have the same aeroelastic behavior. Our results indicated that FG-O plate has the largest stable region with respect to other plates particularly for smaller value of total damping coefficient. The results presented in this paper may be helpful for the aeroelastic analysis of supersonic aero-structures.

Finally, it should be noted that the thermal effect can be included in the aeroelastic analysis of the functionally graded carbon nanotube-reinforced composite plates. This would be an interesting issue for future work.

Appendix

One can determine matrices **A** and **B** by integration as follows.

$$\begin{aligned} \mathbf{A}_{ij} &= \int_0^1 \int_0^1 \mathbf{M}_{ij}\, dX\, dY \\ \mathbf{B}_{ij} &= \int_0^1 \int_0^1 \mathbf{N}_{ij}\, dX\, dY \end{aligned} \qquad i, j = (1, \ldots, 6). \tag{A.1}$$

Components of matrix $\mathbf{M}$ are expressed as

$$
\begin{aligned}
&\mathbf{M}_{ii} = \mathbf{I} \quad (i = 1,3,5) \qquad \mathbf{M}_{ij} = \mathbf{0} \quad (i = 1,3,5 \text{ and } i \neq j)\\
&\mathbf{M}_{22} = H^2 \left(\frac{I_0 E^m}{\rho^m A_1}\right) \boldsymbol{\Phi}_u \boldsymbol{\Phi}_u^T \qquad \mathbf{M}_{26} = -H^2 \left(\frac{I_1 E^m}{\rho^m A_1 a}\right) \boldsymbol{\Phi}_u \frac{\partial \boldsymbol{\Phi}_w^T}{\partial X} \qquad \mathbf{M}_{2j} = \mathbf{0} \quad (j \neq 2,6)\\
&\mathbf{M}_{44} = \frac{H^2}{r^2} \left(\frac{I_0 E^m}{\rho^m B_1}\right) \boldsymbol{\Phi}_v \boldsymbol{\Phi}_v^T \qquad \mathbf{M}_{46} = -\frac{H^2}{r} \left(\frac{I_1 E^m}{\rho^m B_1 a}\right) \boldsymbol{\Phi}_v \frac{\partial \boldsymbol{\Phi}_w^T}{\partial Y} \qquad \mathbf{M}_{4j} = \mathbf{0} \quad (j \neq 4,6)\\
&\mathbf{M}_{62} = -H^2 \left(\frac{I_1 E^m a}{\rho^m A_3}\right) \boldsymbol{\Phi}_w \frac{\partial \boldsymbol{\Phi}_u^T}{\partial X}\\
&\mathbf{M}_{64} = -H^2 r \left(\frac{I_1 E^m a}{\rho^m A_3}\right) \boldsymbol{\Phi}_w \frac{\partial \boldsymbol{\Phi}_v^T}{\partial Y} \qquad \mathbf{M}_{6j} = \mathbf{0} \quad (j \neq 2,4,6)\\
&\mathbf{M}_{66} = -H^2 \left(\frac{I_0 E^m a^2}{\rho^m A_3}\right) \boldsymbol{\Phi}_w \boldsymbol{\Phi}_w^T + H^2 \left(\frac{I_2 E^m}{\rho^m A_3}\right) \left(\boldsymbol{\Phi}_w \frac{\partial^2 \boldsymbol{\Phi}_w^T}{\partial X^2} + r^2 \boldsymbol{\Phi}_w \frac{\partial^2 \boldsymbol{\Phi}_w^T}{\partial Y^2}\right).
\end{aligned}
\tag{A.2}
$$

Moreover, matrix $\mathbf{N}$ can be obtained as

$$
\mathbf{N} = \begin{bmatrix}
\mathbf{0} & \mathbf{I} & \mathbf{0} & \mathbf{0} & \mathbf{0} & \mathbf{0}\\
\mathbf{u_1} & \mathbf{u_2} & \mathbf{u_3} & \mathbf{u_4} & \mathbf{u_5} & \mathbf{u_6}\\
\mathbf{0} & \mathbf{0} & \mathbf{0} & \mathbf{I} & \mathbf{0} & \mathbf{0}\\
\mathbf{v_1} & \mathbf{v_2} & \mathbf{v_3} & \mathbf{v_4} & \mathbf{v_5} & \mathbf{v_6}\\
\mathbf{0} & \mathbf{0} & \mathbf{0} & \mathbf{0} & \mathbf{0} & \mathbf{I}\\
\mathbf{w_1} & \mathbf{w_2} & \mathbf{w_3} & \mathbf{w_4} & \mathbf{w_5} & \mathbf{w_6}
\end{bmatrix}
\tag{A.3}
$$

where $\mathbf{u}_i$, $\mathbf{v}_i$ and $\mathbf{w}_i$ are matrices which represent static coupling of generalized coordinates and are derived as

$$
\begin{aligned}
&\mathbf{u}_1 = \boldsymbol{\Phi}_u \frac{\partial^2 \boldsymbol{\Phi}_u^T}{\partial X^2} + r^2 \left(\frac{C_1}{A_1}\right) \boldsymbol{\Phi}_u \frac{\partial^2 \boldsymbol{\Phi}_u^T}{\partial Y^2} \qquad \mathbf{u}_3 = r \left(\frac{\nu_{12} B_1 + C_1}{A_1}\right) \boldsymbol{\Phi}_u \frac{\partial^2 \boldsymbol{\Phi}_v^T}{\partial X \partial Y}\\
&\mathbf{u}_5 = -\left(\frac{A_2}{A_1 a}\right) \boldsymbol{\Phi}_u \frac{\partial^3 \boldsymbol{\Phi}_w^T}{\partial X^3} - r^2 \left(\frac{\nu_{12} B_2 + 2C_2}{A_1 a}\right) \boldsymbol{\Phi}_u \frac{\partial^3 \boldsymbol{\Phi}_w^T}{\partial X \partial Y^2} \qquad \mathbf{u}_2 = \mathbf{u}_4 = \mathbf{u}_6 = \mathbf{0}\\
&\mathbf{v}_1 = \left(\frac{\nu_{12} B_1 + C_1}{B_1 r}\right) \boldsymbol{\Phi}_v \frac{\partial^2 \boldsymbol{\Phi}_u^T}{\partial X \partial Y} \qquad \mathbf{v}_3 = \frac{1}{r^2} \left(\frac{C_1}{B_1}\right) \boldsymbol{\Phi}_v \frac{\partial^2 \boldsymbol{\Phi}_v^T}{\partial X^2} + \boldsymbol{\Phi}_v \frac{\partial^2 \boldsymbol{\Phi}_v^T}{\partial Y^2}\\
&\mathbf{v}_5 = -r \left(\frac{B_2}{B_1 a}\right) \boldsymbol{\Phi}_v \frac{\partial^3 \boldsymbol{\Phi}_w^T}{\partial Y^3} - \frac{1}{r} \left(\frac{\nu_{12} B_2 + 2C_2}{B_1 a}\right) \boldsymbol{\Phi}_v \frac{\partial^3 \boldsymbol{\Phi}_w^T}{\partial X^2 \partial Y} \qquad \mathbf{v}_2 = \mathbf{v}_4 = \mathbf{v}_6 = \mathbf{0}\\
&\mathbf{w}_1 = -\left(\frac{A_2 a}{A_3}\right) \boldsymbol{\Phi}_w \frac{\partial^3 \boldsymbol{\Phi}_u^T}{\partial X^3} - r^2 a \left(\frac{\nu_{12} B_2 + 2C_2}{A_3}\right) \boldsymbol{\Phi}_w \frac{\partial^3 \boldsymbol{\Phi}_u^T}{\partial X \partial Y^2} \qquad \mathbf{w}_2 = \mathbf{w}_4 = \mathbf{0}\\
&\mathbf{w}_3 = -\left(\frac{B_2 a}{A_3}\right) r^3 \boldsymbol{\Phi}_w \frac{\partial^3 \boldsymbol{\Phi}_v^T}{\partial Y^3} - \left(\frac{\nu_{12} B_2 + 2C_2}{A_3}\right) ar\, \boldsymbol{\Phi}_w \frac{\partial^3 \boldsymbol{\Phi}_v^T}{\partial X^2 \partial Y} \qquad \mathbf{w}_6 = \pi^4 g_T \boldsymbol{\Phi}_w \boldsymbol{\Phi}_w^T\\
&\mathbf{w}_5 = \boldsymbol{\Phi}_w \frac{\partial^4 \boldsymbol{\Phi}_w^T}{\partial X^4} + 2\left(\frac{\nu_{12} B_3 + 2C_3}{A_3}\right) r^2 \boldsymbol{\Phi}_w \frac{\partial^4 \boldsymbol{\Phi}_w^T}{\partial X^2 \partial Y^2} + r^4 \left(\frac{B_3}{A_3}\right) \boldsymbol{\Phi}_w \frac{\partial^4 \boldsymbol{\Phi}_w^T}{\partial Y^4}\\
&\qquad + \lambda \boldsymbol{\Phi}_w \frac{\partial \boldsymbol{\Phi}_w^T}{\partial X} + r_{xx} \boldsymbol{\Phi}_w \frac{\partial^2 \boldsymbol{\Phi}_w^T}{\partial X^2} + r^2 r_{yy} \boldsymbol{\Phi}_w \frac{\partial^2 \boldsymbol{\Phi}_w^T}{\partial Y^2} + 2r r_{xy} \boldsymbol{\Phi}_w \frac{\partial^2 \boldsymbol{\Phi}_w^T}{\partial X \partial Y}.
\end{aligned}
\tag{A.4}
$$

References

[1] T. Prakash, M. Ganapathi, Supersonic flutter characteristics of functionally graded flat panels including thermal effects, Compos. Struct. 72 (2006) 10–18.

[2] H.H. Ibrahim, M. Tawfik, M. Al-Ajmi, Thermal buckling and nonlinear flutter behavior of functionally graded material panels, J. Aircr. 44 (2007) 1610–1618.

[3] K.J. Sohn, J.H. Kim, Structural stability of functionally graded panels subjected to aero-thermal loads, Compos. Struct. 82 (2008) 317–325.
[4] M. Hosseini, S.A. Fazelzadeh, Aerothermoelastic post-critical and vibration analysis of temperature-dependent functionally graded panels, J. Thermal Stresses 33 (2010) 1188–1212.
[5] P. Marzocca, S.A. Fazelzadeh, M. Hosseini, A review of nonlinear aero-thermo-elasticity of functionally graded panels, J. Thermal Stresses 34 (2011) 1–33.
[6] M. Cadek, J.N. Coleman, V. Barron, K. Hedicke, W.J. Blau, Morphological and mechanical properties of carbon-nanotube-reinforced semicrystalline and amorphous polymer composites, Appl. Phys. Lett. 81 (2002) 5123–5125.
[7] E.T. Thostenson, T.W. Chou, On the elastic properties of carbon nanotube-based composites: modelling and characterization, J. Phys. D: Appl. Phys. 36 (2003) 573–582.
[8] K.T. Lau, C. Gu, G.H. Gao, H.Y. Ling, S.R. Reid, Stretching process of single- and multiwalled carbon nanotubes for nanocomposite applications, Carbon 42 (2004) 426–428.
[9] N. Hu, H. Fukunaga, C. Lu, M. Kameyama, B. Yan, Prediction of elastic properties of carbon nanotube reinforced composites, Proc. R. Soc. A-Math. Phys. 461 (2005) 1685–1710.
[10] Y. Han, J. Elliott, Molecular dynamics simulations of the elastic properties of polymer/carbon nanotube composites, Comput. Mater. Sci. 39 (2007) 315–323.
[11] H.S. Shen, Nonlinear bending of functionally graded carbon nanotube-reinforced composite plates in thermal environments, Compos. Struct. 91 (2009) 9–19.
[12] Z.X. Wang, H.S. Shen, Nonlinear vibration of nanotube-reinforced composite plates in thermal environments, Comput. Mater. Sci. 50 (2011) 2319–2330.
[13] P. Zhu, Z.X. Lei, K.M. Liew, Static and free vibration analyses of carbon nanotube-reinforced composite plates using finite element method with first order shear deformation plate theory, Compos. Struct. 94 (2012) 1450–1460.
[14] H.S. Shen, Z.H. Zhu, Postbuckling of sandwich plates with nanotube-reinforced composite face sheets resting on elastic foundations, Eur. J. Mech. A Solids 35 (2012) 10–21.
[15] G. Bhardwaj, A.K. Upadhyay, R. Pandey, K.K. Shukla, Non-linear flexural and dynamic response of CNT reinforced laminated composite plates, Composites B 45 (2013) 89–100.
[16] Z.X. Lei, K.M. Liew, J.L. Yu, Large deflection analysis of functionally graded carbon nanotube-reinforced composite plates by the element-free kp-Ritz method, Comput. Methods Appl. Mech. Engrg. 256 (2013) 189–199.
[17] E. Abdollahzadeh Shahrbabaki, A. Alibeigloo, Three-dimensional free vibration of carbon nanotube-reinforced composite plates with various boundary conditions using Ritz method, Compos. Struct. 111 (2014) 362–370.
[18] L.W. Zhang, Z.X. Lei, K.M. Liew, J.L. Yu, Large deflection geometrically nonlinear analysis of carbon nanotube-reinforced functionally graded cylindrical panels, Comput. Methods Appl. Mech. Engrg. 273 (2014) 1–18.
[19] Z.X. Lei, L.W. Zhang, K.M. Liew, J.L. Yu, Dynamic stability analysis of carbon nanotube-reinforced functionally graded cylindrical panels using the element-free kp-Ritz method, Compos. Struct. 113 (2014) 328–338.
[20] K.M. Liew, X. Zhao, A.J.M. Ferreira, A review of meshless methods for laminated and functionally graded plates and shells, Compos. Struct. 93 (2011) 2031–2041.
[21] G.D. Seidel, D.C. Lagoudas, Micromechanical analysis of the effective elastic properties of carbon nanotube reinforced composites, Mech. Mater. 38 (2006) 884–907.
[22] B. Sobhani Aragh, A.H. Nasrollah Barati, H. Hedayati, Eshelby–Mori–Tanaka approach for vibrational behavior of continuously graded carbon nanotube-reinforced cylindrical panels, Composites B 43 (2012) 1943–1954.
[23] J.D. Fidelus, E. Wiesel, F.H. Gojny, K. Schulte, H.D. Wagner, Thermo-mechanical properties of randomly oriented carbon/epoxy nanocomposites, Composites A 36 (2005) 1555–1561.
[24] A.M.K. Esawi, M.M. Farag, Carbon nanotube reinforced composites: potential and current challenges, Mater. Des. 28 (2007) 2394–2401.
[25] K.M. Liew, Z.X. Lei, J.L. Yu, L.W. Zhang, Postbuckling of carbon nanotube-reinforced functionally graded cylindrical panels under axial compression using a meshless approach, Comput. Methods Appl. Mech. Engrg. 268 (2014) 1–17.
[26] E.H. Dowell, Aeroelasticity of Plates and Shells, Noordhof, Leyden, 1975.
[27] H. Ashley, G. Zartarian, Piston theory—a new aerodynamic tool for the aeroelastician, J. Aeronaut. Sci. 23 (1956) 1109–1118.
[28] J.M. Hedgepeth, Flutter of rectangular simply supported panels at high supersonic speeds, J. Aeronaut. Sci. 24 (1957) 563–573.
[29] S.C. Dixon, Comparison of panel flutter results from approximate aerodynamic theory with results from exact theory and experiment, NASA TN D-3649, 1966.
[30] J.C. Houbolt, A Study of Several Aerothermoelastic Problems of Aircraft Structures in High Speed Flight, Verlag Leemann, Zurich, 1958.
[31] M. Amabili, Nonlinear Vibrations and Stability of Shells and Plates, Cambridge University Press, New York, 2008.
[32] J. Dugundji, Theoretical considerations of panel flutter at high supersonic Mach numbers, AIAA J. 4 (1966) 1257–1266.
[33] D.K. Jha, Tarun Kant, R.K. Singh, Free vibration response of functionally graded thick plates with shear and normal deformations effects, Compos. Struct. 96 (2013) 799–823.